High-energy X-ray Tomography for 3D Void Characterization in Au–Sn Solid-Liquid Interdiffusion (SLID) Bonds

Knut E. Aasmundtveit[1,2*], Kim Robert Tekseth[3], Dag W. Breiby[1,3], Hoang-Vu Nguyen[1]

[1] Dept. of Microsystems, University of South-Eastern Norway, 3184 Borre, Norway
[2] Dept. of Physics, Norwegian University of Science and Technology (NTNU), 7491 Trondheim, Norway
[3] PoreLab, Dept. of Physics, Norwegian University of Science and Technology (NTNU), 7491 Trondheim, Norway

Phone: +47-3100 9658, and E-mail Address: kaa@usn.no

Abstract

Au–Sn SLID bonding is a technique originally developed for harsh environment applications. The technology has recently shown promising results for ultrasound transducer fabrication. Characterizing the spatial and size distributions of voids is crucial for developing a fabrication process that satisfies acoustic requirements. This measurement is traditionally done by optical or electron cross-section microscopy that gives the void distribution in a randomly selected physically cut plane. X-ray micro computed tomography is a powerful tool for non-destructive three-dimensional imaging of void distributions, but is challenging to use in high-density materials like the ones used in ultrasound transducers.
We demonstrate that monochromatic, high-energy synchrotron X-ray tomography can give 3D images of such a challenging sample, resolving μm-sized voids in the bondline. The void distribution is highly non-uniform, implying that traditional cross-section microscopy would give different results depending on the plane of sectioning. Computed tomography allows the voids to be parametrized and treated statistically, revealing a wide distribution of void sizes, a tendency to form oblate voids with size-dependent orientation, as well as porous networks.

Key words: SLID bonding; X-ray Tomography; electro-acoustic devices; PZT; voids in bonding

I. Introduction

Solid-Liquid Interdiffusion (SLID) bonding is a technique based on a binary or ternary metal system that transforms to high-temperature stable intermetallic compounds (IMCs) at moderate bonding temperatures [1, 2]. Cu–Sn [3-5] and Au–Sn [6-8] are the most studied SLID systems, with processing temperatures above 232 °C and 278 °C, and with IMCs melting at about 700 °C and 500 °C, respectively. Initially developed for harsh environment applications, SLID bonding has proved to provide well-defined thin-layer metallurgical bonds, as well as excellent robustness [9] and possibility for fine-pitch bonding [3, 5]. The low to moderate bonding temperatures also enables the use of SLID bonding for temperature-sensitive materials such as poled piezoelectric materials, polymers and ferromagnets.

We have previously demonstrated Au–Sn and Au–In–Bi SLID bonding for ultrasound applications [10, 11]. The desired properties are thin-layer metallurgical bonds, with acoustic impedance matched to the bonding partners. For this application, the amount of voids in the bond must be minimized, as acoustic waves scatter at these voids. The standard method to characterize voids in the bond is through cross-section microscopy. We have previously compared such cross-sections with electrical impedance spectroscopy in order to investigate what level of voiding can be accepted for given acoustic requirements [12]. However, cross-section microscopy is a destructive technique, and it only gives 2D information from the chosen cross-section surface. Whether this cross-section surface is representative for the sample, remains an open question.

In this work, we have used X-ray tomography to access 3D information of the voids in the bonding layer of an ultrasound transducer dummy sample. The sample studied is a Lead Zirconate Titanate (PZT) die bonded to a Resonant Backing Layer (RBL) substrate using Au–Sn SLID bonding. The tomography data are compared with cross-section microscopy of samples manufactured with the same process.

The transducer sample is challenging to measure using X-ray computed tomography (CT) owing to the heavy elements (including lead and zirconium) giving strong absorption of the X-ray beam. For this reason, earlier attempts at using synchrotron CT with a modest beam energy of about 20 keV were unsuccessful. Similarly, despite the high maximum photon energy of home laboratory setups (e.g. Nikon XT H 225 ST, with photon energies ranging upto 225 keV), the polychromatic

design of these instruments gives reduced resolution and weak contrast. For these reasons, CT setups based on monochromatic high-energy X-rays, as available at a few synchrotron beamlines around the world, are needed to image these mm-sized transducer samples in 3D. To the best of our knowledge, other imaging techniques cannot non-destructively resolve the internal µm-sized voids in the bonding layer. Scanning Acoustic Microscopy (SAM) is an alternative technique for non-destructive 3D imaging of voids, but the high acoustic impedance of PZT and RBL reflects the acoustic probing signal, limiting the signal-to-noise ratio and resolution obtained.

II. Experimental

A. Test vehicles

1) Materials

The test samples consisted of a PZT die bonded to a tungsten carbide-based RBL substrate using a eutectic Au–Sn preform. The dies had dimensions 5 × 5 mm^2 with Au coated on both sides. On the bonding side, the Au layer was electroplated to a thickness of 10-13 µm. The absolute roughness of the dies' bonding surface was in the range 1.2-1.5 µm. The substrates had dimensions slightly larger than the dies to facilitate the bonding process. The electroplated Au layer on the bonding side of the substrates had a thickness in the range 10-12 µm. The absolute roughness of the substrates' bonding surface was in the range 0.3-0.5 µm. No patterning was applied to the bonding surfaces of the dies and the substrates. The eutectic Au–Sn (Au 80 wt% - Sn 20 wt%) preform used in this work was supplied by Indium Corporation (USA). The preform had a thickness of about 25 µm, and was cut to dimensions suitable for bonding.

The Au thickness on the bonding side of the PZT dies and the RBL substrates, as well as the preform thickness, were selected to assure a surplus of Au in the bond-layer. The chosen thickness values of the different parts result in bonds with a layered structure of Au / Au–Sn (ζ phase) / Au, which has been reported to provide Au–Sn bonds with high mechanical strength and long-time reliability [9]. Note that the ζ phase is Au-rich, containing 8-16 at% / 5-10 wt% Sn.

2) Bonding process

Prior to bonding, PZT dies and RBL substrates were cleaned using an ultrasonic bath. The eutectic Au–Sn preform surfaces were cleaned on both sides with N_2 airflow to blow off dust particles (if present).

For each sample, a piece of Au–Sn preform was sandwiched between a die and a substrate. The substrate, the preform and the die were manually aligned on a flat ceramic heater. Next, the entire sample was kept fixed on the heater using a clamp, and was put inside a vacuum chamber. A bonding temperature profile was then applied under the control of a programmable PID controller (EZ-ZONE PM, Watlow, USA). The temperature profile applied included two main steps:

i) Heating a sample from room temperature to 250 °C and maintaining the temperature for 5 minutes to bake out any residual moisture and to assure a uniform temperature distribution in the bonding layers. Additionally, initial bonding is formed by solid-state diffusion, ensuring that the subsequent bonding will proceed with uniform growth of IMC layers [13].

ii) Heating the sample from 250 °C to the final bonding temperature of about 310 °C and maintaining the temperature for 15 minutes. After that, the sample is cooled down to room temperature.

B. Characterization

1) Synchrotron X-ray Computed Tomography

The X-ray measurement of the transducer sample of external dimensions 5 × 0.5 × 0.4 mm^3 (diced from the originally bonded sample for optimal tomography resolution) was carried out at the high-energy CT beamline ID19 [14, 15] at the European Synchrotron Radiation Facility (ESRF) in Grenoble, France. The transducer sample was placed on a goniometer and illuminated with a parallel monochromatic X-ray beam with a photon energy of 68 keV. Approximately 2000 projections were acquired at equally spaced angles by rotating the sample about a vertical axis perpendicular to the beam. The measurement geometry used corresponds to an isotropic voxel size of 1.39 µm. The actual resolution was at least a factor 2-3 lower. The 3D reconstruction was obtained with the filtered back-projection reconstruction algorithm. The 3D volume was filtered using a wavelet-FFT filter [16] to reduce the presence of ring artifacts while retaining the structural information. Finally, segmentation using simple thresholding was used to separate voids from the sample phases. Statistics of the pore properties were obtained using Matlab®.

2) Cross-section microscopy

Open cross sections for microscopy of the bonded samples (PZT-RBL) were prepared using a conventional cross-sectioning process followed by Ar ion milling (IM4000, Hitachi High-Technologies, Japan). The bondline of the samples was inspected by optical microscopy (NEOPHOT 32, Jenoptik Jena GmbH, Germany), as well as scanning electron microscopy (SEM) and energy dispersive X-ray spectroscopy (EDX) (SU3500, Hitachi High-Technologies, Japan).

III. Representative Cross-sections – Tomography and Microscopy

A. X-ray Tomography

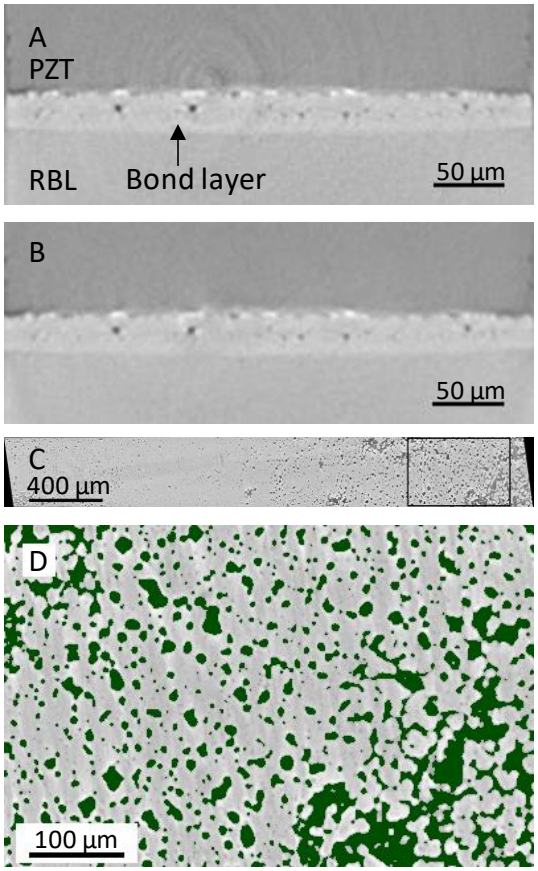

Figure 1: Reconstructed X-ray tomograms. A) Cross-section displaying the PZT die, RBL substrate and bond layer. B) Processed cross-section using wavelet-FFT filtering to remove ring artifacts. C) Reconstructed cross-section revealing the distribution of voids in the bond layer (cross-section normal to the one in A). The black wedges correspond to regions outside the field of view. D) Magnified cross-section of C, highlighting the segmented voids in dark/ green.

Figure 1 shows reconstructed X-ray tomograms, representing virtual cross-sections at different locations and for different orientations in the sample. It is clearly seen that the high photon energy in use (68 keV) gives a good material-specific contrast and signal-to-noise ratio, despite the high absorption in all three layers of the sandwich structure, namely PZT, Au/ Au–Sn, and RBL.

The reconstructed cross-section normal to the bond plane, cf. Figure 1 A), corresponds to a traditional cross-section micrograph. The bondline is clearly distinguished from the PZT and RBL layers, and voids can clearly be discerned in the bondline. The ring patterns are a common artefact in computed tomography. Figure 1 B) represents the same reconstructed cross-section, at the same position as the one in Figure 1 A), after wavelet FFT filtering. Evidently, the ring artefacts are suppressed, without deterioration of the structural information. Suppression of the ring artefacts allows a more precise determination and analysis of the voids in the bond layer.

Figure 1 C-D) show reconstructed cross-sections in the bond layer, revealing information that is not readily available in traditional cross-section micrographs. The voids have a broad size distribution, and the void density is highly non-uniform. This implies that the information obtained through conventional cross-section micrographs would exhibit a large variation, depending on the position where the sample is cross-sectioned.

B. Cross-section microscopies

An optical micrograph of a cross-sectioned sample, manufactured with similar parameters as the one used for X-ray tomography, is given in Figure 2. Figure 2 A) has the same magnification as Figure 1 A-B, and the two techniques indeed give similar results in terms of bond layer shape and dimensions, as well as the spatial and size distributions of the voids. Figure 2 B) shows a magnified view, with a high-resolution objective (NA = 0.9). The optical micrograph can resolve smaller voids than our X-ray tomography setup allows, limited only by the diffraction limit of the microscope in use. Figure 2 B) resolves voids with dimensions down to ~0.3 µm. Note also the good material contrast obtained in the optical micrographs, easily distinguishing Au from Au–Sn intermetallics. Since all the materials in the sample are high-density materials, the overall material contrast is less pronounced in the X-ray tomography measurements.

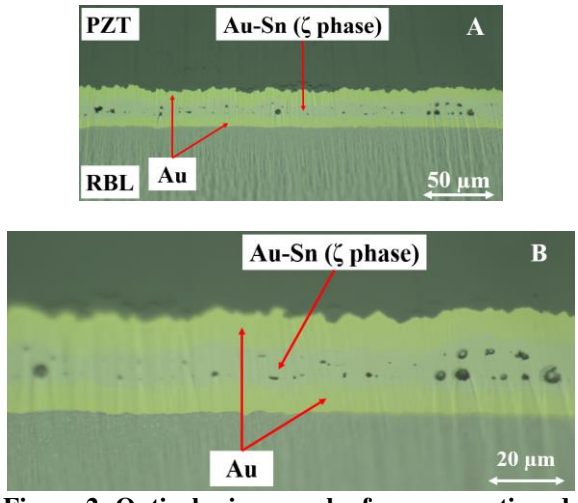

Figure 2: Optical micrograph of a cross-sectioned sample, being similar to the sample in Figure 1. A) Same scale as in Figure 1 A-B, showing comparable results. B) Magnified view. Small voids are observed in the bond layer, with sub-µm resolution. Reproduced from [12].

Scanning electron microscopy of cross-sections is able to resolve even smaller voids. Figure 3 shows a SEM micrograph of a Au–Sn SLID bonded model transducer. The image has a moderate magnification, still resolving voids < 0.1 µm. Note that the material contrast is much lower than in the optical micrograph, being primarily a channeling contrast differentiating crystal orientations of grains (exposing the difference between small-grain sputtered Au seed layer and large-grain Au electroplated layers). More details on contrast for studies of SLID bonds can be found in our previous publication [17].

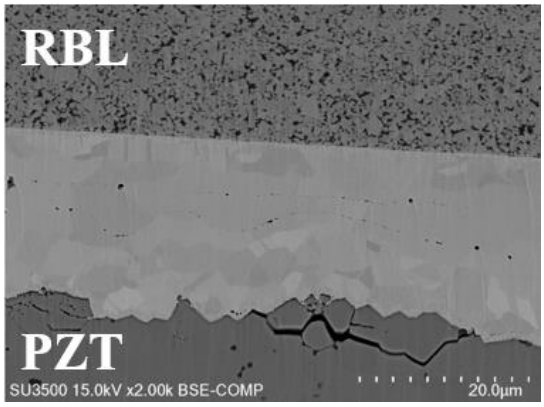

Figure 3: SEM micrograph of a cross-sectioned sample Au–Sn SLID bonded sample, with Au / Au–Sn / Au SLID bond between RBL and PZT.

IV. 3D Analysis of Void Content

The power of X-ray tomography lies in the ability to extract 3D microscopic images from a sample non-destructively, allowing detailed analysis of the internal structures in the sample.

A. Void parameterization

The voids were labeled using a connectedness of 6, meaning that two neighbouring void voxels will be considered to belong to the same void only if they are face-to-face connected. Considering the experimental uncertainty relating to the resolution and the contrast, only voids consisting of more than 9 voxels were included in the analysis. With an isotropic voxel size of 1.4 µm, this corresponds to a minimum void size of 27 μm^3 for inclusion in the statistical analysis. For consistency with the limited resolution, the few voids having only one voxel width along one dimension were discarded.

For a statistical analysis that reflects the dimension, shape and orientation of the voids, each void was parameterized as an ellipsoid, with three principal axes $\mathbf{p}_1$, $\mathbf{p}_2$, $\mathbf{p}_3$ each defined as having the same second central moment as the void. The length and orientation of these three principal axes were used as the model parameters to describe each void. Note that $\mathbf{p}_1$ is taken to be the longest principal axis of the void, and $\mathbf{p}_3$ the shortest – their orientation with respect to the sample geometry is defined through Euler angles yaw, pitch and roll.

B. Number and volume of voids

When labeling voids using a connectedness of 6, a total of about 6300 voids were detected in the bonding layer volume. This number was reduced to ~3100 labeled voids by only considering those voids consisting of more than 9 voxels. These ~3100 voids correspond to an estimated void fraction of the bond layer of 4 %. The single largest void contributed approximately 10 % of the total pore volume, while 50 % of the total pore volume could be accounted for by the 54 largest voids.

Figure 4 shows the normalized cumulative void volume: The voids are sorted from the largest (#1) to the smallest, and for each void the volume is normalized towards the total volume of voids in the bond layer. It can easily be read from Figure 4 that the largest void indeed accounts for 10 % of the total void volume, and that the 10-11 largest voids contribute 40 % of the total volume.

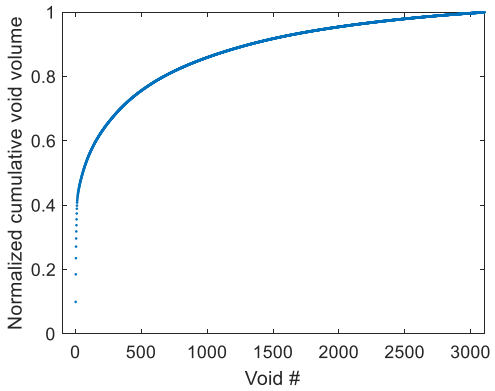

Figure 4: Normalized cumulative void volume.

C. Principal axes – length and orientation

The principal axes lengths exhibit a large distribution: The mean principal axis lengths were 9 µm ($\mathbf{p}_1$), 6 µm ($\mathbf{p}_2$) and 4.5 µm ($\mathbf{p}_3$), while the longest principal axes were 292 µm, 184 µm and 13 µm. The much lower maximum value for $\mathbf{p}_3$ is compatible with the void size being restricted in one dimension by the actual bond layer thickness. Figure 5 gives the distribution of principal axes lengths, showing the data for axes of length < 25 µm.

Figure 6 shows the orientation distribution of $\mathbf{p}_1$, for the 200 largest voids as well as for the remaining smaller voids. Void #200, selected to differentiate between large and small voids in Figure 6, has principal axis lengths 13.8 µm ($\mathbf{p}_1$), 8.3 µm ($\mathbf{p}_2$) and 7.5 µm ($\mathbf{p}_3$). The yaw angle is uniformly distributed for both data sets, whereas the pitch and roll angles exhibit qualitatively different distributions for the large and the small voids.

The bond layer thickness imposes a constraint on the void extension, implying that large voids must have their long principal axes in-plane, as seen in the data. Notably, also the small voids are seen to exhibit a preferred orientation. The largest voids are oblate with $p_1 \sim p_2 >> p_3$. The long axes are necessarily oriented in the bonding plane, confined by the ~15 µm thickness of the bonding layer. If looking at only the largest voids (selecting a larger void than #200 for defining large voids), this orientation distribution would be even narrower than the one presented in Figure 6. The smaller voids (#200 - #3000) also tend to be non-spherical and oriented, however with the long axis perpendicular to the bonding layer.

While the largest voids have a solidity of about 0.6, voids from about #2000 (p_1 = 9.7 µm, p_2 = 5.3 µm, p_3 = 2.2 µm) have a solidity near unity, meaning they are homogeneous objects.

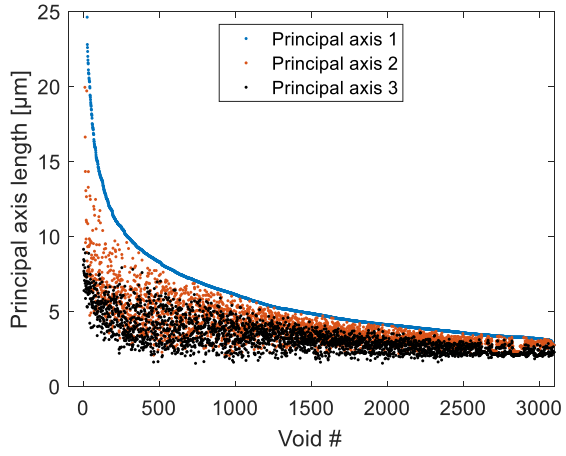

Figure 5: Principal axis lengths in descending order of the longest principal axis p_1.

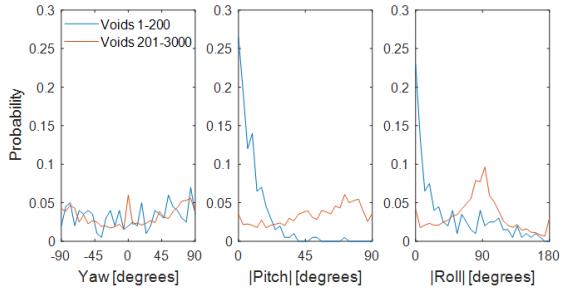

Figure 6: Orientation of the longest principal axis (p_1), for the 200 largest voids and for the remaining smaller voids. The yaw orientation distribution exhibits no preferred orientation. The pitch and roll angle distributions clearly signify that for the large voids, *both* the longest and second longest principal axes (p_1 and p_2) tend to be oriented parallel to the bonding layer. Also small voids are oriented, but with their longest principal axis (p_1) perpendicular to the bonding layer.

D. Larger voids vs smaller voids

From the distributions shown above, it is clear that the majority of voids has a moderate size and follows well-defined distributions where a statistical approach may be appropriate. The large voids are statistical outliers. Hence, it is appropriate to investigate these individually. Figure 7 shows orthogonal views of the largest void detected, false-colored red. This large void appears to be a connected network of smaller voids.

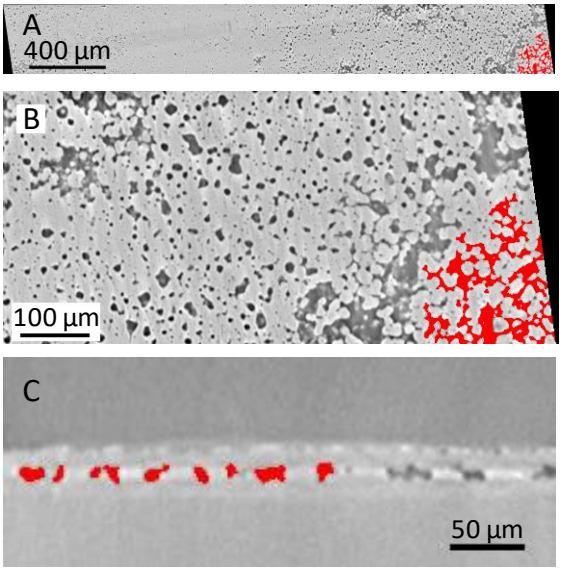

Figure 7: Reconstructed X-ray tomograms, showing the largest void in the sample, highlighted in red. A) Cross-section in the bond plane. The black wedges correspond to regions outside the field of view. B) Magnified cross-section in the bond plane. C) Cross-section normal to the bond plane.

For a statistical treatment of the moderately sized voids, we omitted the large voids accounting for about 50% of the total void volume, cf. Figure 4. This gave a cutoff at about 450 voxels from the analysis, corresponding to omitting the 66 largest voids from the analysis. The maximum principal axis lengths in the truncated data set were $p_{1,max}$ = 34 µm, $p_{2,max}$ = 15 µm, $p_{3,max}$ = 11 µm. The mean values of the principal axis lengths do not change much compared with the data set including all voids, but the standard deviation is now a relevant number. The mean values and standard deviations for the principal axis lengths are p_1 = (8 ± 4) µm, p_2 = (5.5 ± 1.9) µm, p_3 = (4.4 ± 1.4) µm.

V. Discussion

The three-dimensional nature of tomography measurements gives access to vastly more information than what is obtainable from traditional cross-section microscopy. The tomography

measurements and analysis reported in this paper, reveal a sample with a highly inhomogeneous void distribution, and a broad distribution of void sizes. This implies that cross-section microscopy would give qualitatively different results depending on the actual position where the sample is cross-sectioned. Comparing Figure 1 B and Figure 7 C gives a clear indication how different two reconstructed cross-sections from the same sample can be, where the only difference is the position of the reconstructed plane. The three-dimensional nature of the tomography data also allows a straightforward reconstruction of in-plane cross-sections, clearly imaging the spatial distribution of voids. Mapping such inhomogeneity through cross-section microscopy would require a large number of physically cut cross-sections. The destructive nature limits how many cross-sections can be made, and thus limits the amount of information that can possibly be retrieved.

Comparing Figure 1 B and Figure 2 A demonstrates that X-ray tomography and cross-section microscopy indeed give comparable results, if a corresponding reconstructed cross-section is selected from the tomography data. This comparison is therefore important, since it validates the accuracy of the information retrieved from the tomography data. The advantages of cross-section microscopies include the easy instrument access, higher resolution and better material contrast, as well as being a well-established and recognized technique for bond characterization.

Tomography reveals large voids and complex porous networks that would not be observable in a randomly cut cross-section, whereas cross-section microscopy reveals small voids that cannot be resolved with the X-ray tomography setup used. Our analysis of 3D void distribution in the bond layer can thus take into account only the voids that are larger than 3-4 µm. For ultrasound transducer applications, it is the larger voids that will most severely impede the acoustical performance. We have previously demonstrated by comparing cross-section microscopy with electrical impedance spectroscopy that a bond can have a distribution of smaller voids without sacrificing the acoustical performance [12]. The relevant length scale for what should be considered small or large voids, is the ultrasound wavelength for the application.

Uniformity, homogeneity and reproducibility are required for industrial manufacturing processes. For a mature process where a high uniformity and homogeneity are achieved, cross-section microscopy will remain a highly relevant characterization method. We have shown here that X-ray tomography gives unique information for process development, by providing 3D image data for an inhomogeneous sample.

VI. Conclusions

Synchrotron-based X-ray tomography gave non-destructive three-dimensional information about the void content in the bond layer of a Au–Sn SLID bonded ultrasound transducer dummy sample. Using high-energy monochromatic X-rays, as enabled by the selected synchrotron beamline, allows high-quality tomograms to be retrieved despite the high X-ray absorption of the sample being rich in high-density materials.

The tomography data exhibited a highly inhomogeneous void distribution, and a large variation in void sizes. Statistical analysis of void size, shape and orientation can be retrieved, information that is not obtainable by traditional cross-section microscopy. We have demonstrated the arbitrariness inherent in a cross-section analysis of an inhomogeneous sample, and propose X-ray tomography as a valuable tool in manufacturing process development.

Acknowledgements

The authors thank Zekija Ramic and Anh-Tuan Thai Nguyen, both USN, for Au electroplating of samples, and Tung Manh (USN) and Trym Eggen (GE Vingmed Ultrasound AS) for valuable discussions.

The present work was funded by the Research Council of Norway through the NANO2021 program (project number 235302; B-EAM – Advanced Assembly Technologies for Electro Acoustic Module used in Ultrasound Cardiovascular Applications). The Research Council of Norway is also acknowledged for the support to the Norwegian Micro- and Nano-Fabrication Facility, NorFab, project number 245963.

KRT and DWB thank the Research Council of Norway for funding through its Centres of Excellence scheme (project 262644) and FRINATEK (project 275182).

References

[1] K. E. Aasmundtveit, T.-T. Luu, H.-V. Nguyen, A. Larsson, and T. A. Tollefsen, "Intermetallic Bonding for High-Temperature Microelectronics and Microsystems: Solid-Liquid Interdiffusion Bonding," in *Intermetallic Compounds - Formation and Applications*, M. Aliofkhazraei, Ed., ed Open Access: Intech Open, 2018.

[2] L. Bernstein, "Semiconductor joining by solid-liquid-interdiffusion (SLID) process.," *Journal of the Electrochemical Society,* vol. 113, pp. 1282-88, 1966.

[3] H. Huebner, S. Penka, B. Barchmann, M. Eigner, W. Gruber, M. Nobis*, et al.*, "Microcontacts with sub-30 µm pitch for 3D chip-on-chip integration," *Microelectronic Engineering,* vol. 83, pp. 2155-2162, Nov-Dec 2006.

[4] T. T. Luu, A. Duan, K. E. Aasmundtveit, and N. Hoivik, "Optimized Cu-Sn wafer-level bonding using intermetallic phase characterization," *Journal of Electronic Materials,* vol. 42, pp. 3582-3592, 2013.

[5] C. Honrao, T. C. Huang, M. Kobayashi, V. Smet, P. M. Raj, and R. Tummala, "Accelerated SLID bonding using thin multi-layer copper-solder stack for fine-pitch interconnections," in *2014 IEEE 64th Electronic Components and Technology Conference (ECTC)*, 2014, pp. 1160-1165.

[6] T. A. Tollefsen, A. Larsson, O. M. Lovvik, and K. Aasmundtveit, "Au-Sn SLID Bonding-Properties and Possibilities," *Metallurgical and Materials Transactions B-Process Metallurgy and Materials Processing Science,* vol. 43, pp. 397-405, Apr 2012.

[7] W. R. Johnson, C. Q. Wang, Y. Liu, and J. D. Scofield, "Power Device Packaging Technologies for Extreme Environments," *IEEE Transactions on Electronics Packaging Manufacturing,* vol. 30, pp. 182-193, 2007.

[8] A. Rautiainen, H. B. Xu, E. Osterlund, J. Li, V. Vuorinen, and M. Paulasto-Krockel, "Microstructural Characterization and Mechanical Performance of Wafer-Level SLID Bonded Au-Sn and Cu-Sn Seal Rings for MEMS Encapsulation," *Journal of Electronic Materials,* vol. 44, pp. 4533-4548, Nov 2015.

[9] T. A. Tollefsen, A. Larsson, M. M. V. Taklo, A. Neels, X. Maeder, K. Hoydalsvik*, et al.*, "Au-Sn SLID Bonding: A Reliable HT Interconnect and Die Attach Technology," *Metallurgical and Materials Transactions B-Process Metallurgy and Materials Processing Science,* vol. 44, pp. 406-413, Apr 2013.

[10] T. Manh, H. V. Nguyen, D. Le-Anh, K. Aasmundtveit, L. Hoff, T. Eggen*, et al.*, "Au-Sn Solid-Liquid Interdiffusion (SLID) bonding for piezoelectric ultrasonic transducers," in *2016 IEEE International Ultrasonics Symposium (IUS)*, 2016, pp. 1-4.

[11] K. E. Aasmundtveit, T. Eggen, T. Manh, and H. V. Nguyen, "In-Bi low-temperature SLID bonding for piezoelectric materials," *Soldering & Surface Mount Technology,* vol. 30, pp. 100-105, 2018.

[12] H. V. Nguyen, M. Tung, T. Eggen, and K. E. Aasmundtveit, "Au-Sn Solid-Liquid Interdiffusion (SLID) bonding for mating surfaces with high roughness," in *2016 6th Electronic System-Integration Technology Conference (ESTC)*, 2016, pp. 1-6.

[13] H. Etschmaier, H. Torwesten, H. Eder, and P. Hadley, "Suppression of Interdiffusion in Copper/Tin Thin Films," *Journal of Materials Engineering and Performance,* vol. 21, pp. 1724-1727, 2012/08/01 2012.

[14] E. Boller, P. Tafforeau, A. Rack, V. Fernandez, L. Helfen, M. Rénier*, et al.*, "Synchrotron-tomography with micro, nano and high temporal resolution for industrial and academic use," presented at the 3rd International Conference on Tomography of Materials and Structures, Lund, Sweden, 2017.

[15] T. Weitkamp, P. Tafforeau, E. Boller, P. Cloetens, J. P. Valade, P. Bernard*, et al.*, "Status and evolution of the ESRF beamline ID19," *AIP Conference Proceedings,* vol. 1221, pp. 33-38, 2010.

[16] B. Munch, P. Trtik, F. Marone, and M. Stampanoni, "Stripe and ring artifact removal with combined wavelet - Fourier filtering," *Optics Express,* vol. 17, pp. 8567-8591, May 2009.

[17] K. E. Aasmundtveit, H. Jiang, T. A. Tollefsen, T. Luu, and H. Nguyen, "Phase Determination in SLID Bonding," in *2018 7th Electronic System-Integration Technology Conference (ESTC)*, 2018, pp. 1-6.